

Low-divergence relativistic proton jet from a thin solid target driven by an ultra-intense circularly polarized Laguerre–Gaussian laser pulse

Ki Hong Pae^{1,2} , Hoon Song^{1,3} , Chang-Mo Ryu¹ ,
Chang Hee Nam^{1,3}  and Chul Min Kim^{1,2} 

¹Center for Relativistic Laser Science, Institute for Basic Science, Gwangju 61005, Republic of Korea

²Advanced Photonics Research Institute, Gwangju Institute of Science and Technology, Gwangju 61005, Republic of Korea

³Department of Physics and Photon Science, Gwangju Institute of Science and Technology, Gwangju 61005, Republic of Korea

E-mail: chulmin@gist.ac.kr

Received 14 January 2020, revised 27 February 2020

Accepted for publication 5 March 2020

Published 30 March 2020



Abstract

We propose a new ion acceleration scheme of irradiating a thin solid target with an ultraintense circularly polarized Laguerre–Gaussian (LG) laser pulse. Three-dimensional particle-in-cell simulations are performed to demonstrate that this scheme can generate a low-divergence high-density relativistic proton jet. By this scheme, the number of protons emitted with a small angle ($<1^\circ$) from the laser axis can be more than tens of times as high as that of the protons accelerated by a circularly polarized Gaussian pulse. The inward ponderomotive force of the LG pulse drives such a proton beam along the laser axis.

Keywords: radiation pressure acceleration, Laguerre–Gaussian pulse, laser-driven ion acceleration

(Some figures may appear in colour only in the online journal)

1. Introduction

As high-power lasers move into the ultrahigh-intensity regime, a novel scheme of laser-ion acceleration has appeared, which is called radiation pressure acceleration (RPA). In this scheme, ions are accelerated not by the plasma sheath field but by the systematic charge separation field induced by the laser field's enormous radiation pressure [1, 2]. When an ultra-intense laser pulse is incident on a sufficiently thin solid foil, the whole foil is ionized simultaneously. Then the electrons are pushed forward immediately leaving the ions behind because the ponderomotive acceleration of electrons is larger than that of ions by an enormous factor of $(m_i/m_e)^2$, where m_i and m_e are masses of electrons and ions, respectively. The resulting charge separation field can tug the ions to a very high energy. Such charge separation

structure can be maintained well as far as the laser pulse is reflected by the plasma. Through the whole process, the momentum of the laser radiation is transferred eventually to the ions through the mediation of the charge separation field. Because the laser energy is converted little to the plasma's thermal energy, the RPA is expected to be highly efficient, especially as compared to the scheme utilizing the plasma sheath field. Although RPA should work regardless of laser polarization [3, 4], the case of circular polarization has been investigated more popularly than the case of linear polarization because, lacking a longitudinal oscillation, circularly polarized laser pulses provide a more stable charge separation structure and are effective at the lower laser intensities that are experimentally available [5–9]. In experiments, the features of RPA such as narrower spectra, existence of optimum condition, and scaling of maximum energy to laser intensity were

demonstrated [10–13], and an achievement of proton energy of around 90 MeV was reported [13].

Despite these conceptual attraction and promising results, the RPA has several limiting factors such as sensitive dependence on laser and target condition, and inherent plasma instabilities. Some ideas have been proposed to understand and overcome the limiting factors [14–16]. In addition to these limiting factors, high beam divergence is also an important problem because it necessitates a heavy ion focusing system, spoiling the advertised compactness of laser-ion accelerators [17]. However, little attention has been paid to this problem.

To reduce the beam divergence, a radially inward ponderomotive force is required, which can be obtained from a hollow beam profile. A combination of TEM modes can provide such a profile, and its use for electron acceleration was proposed [18]. However, a simpler and well-established way is to use Laguerre–Gaussian (LG) beam modes [19, 20]. LG modes have been studied for more than two decades due to their unique capability of carrying an orbital angular momentum (OAM) of radiation [21], which has led to many applications involving the rotational aspects of light–matter interactions [22]: transfer of laser’s angular momentum (AM) to absorptive particles [23], generation of high-order vortex harmonics [24, 25] and their application to plasma holograms [26], and laboratory emulation of rotating black holes [27, 28]. In contrast, the use of the hollow beam profile has been relatively rare although it was considered for confining the plasma plume from a laser-irradiated solid surface [29], boosting the energy of energetic protons in an underdense plasma [30], and generating ultrashort electron bunches from micro-droplets, nano-wires, and nano-fibers [31–33]. Recently, LG laser pulses were used in a laser-proton acceleration experiment in the target normal sheath regime, which showed a reduction of proton divergence and an enhancement of proton energy albeit to a modest degree [34]. In the RPA regime, few experiments or simulations exploiting the hollow beam profile of LG pulses have been reported.

Here, we propose a novel ion acceleration scheme based on an intense LG laser pulse irradiating an ultrathin solid target, where we utilize the unique characteristics of the LG pulse having a hollow intensity profile. Such an intensity profile can provide an effective ponderomotive force to push the ions toward the laser axis, thereby dramatically reducing the divergence of the ion beam. This effect becomes stronger with the increase of laser intensity, especially in the ultrahigh-intensity regime. Performing 3D particle-in-cell (PIC) simulations, we demonstrate that a low-divergence high-density proton jet can be generated by using a circularly polarized LG pulse. In our study, it is shown that the number of high-energy protons increases by a factor of more than tens for an emission angle smaller than 1° , compared with the conventional RPA using a circularly polarized Gaussian pulse. The resulting high-energy low-divergence proton jet would have a wide range of applications in future ion accelerators.

2. Methods

We conducted 3D relativistic PIC simulations of a solid-density plasma foil onto which an ultra-intense circularly polarized LG laser pulse is incident. In principle, such a configuration can be obtained by putting a helical phase plate in the path of a circularly polarized Gaussian pulse that is incident on the target. The optical thickness of the helical phase plate changes by a multiple (l) of the laser wavelength under one rotation around the beam axis (the z axis below). In practice, transmissive plates are not suitable for high-power radiation, and mirrors with a spirally varying thickness have been proposed for high-power radiation [35]. The resulting LG mode is expressed in cylindrical coordinates (r, θ, z) as follows [20, 32, 36]:

$$\mathbf{E}_\perp(r, \theta, z; l, s) = E(r, z; l) [\sin(\eta + l\theta)\hat{\mathbf{x}} + s \cos(\eta + l\theta)\hat{\mathbf{y}}] / \sqrt{2} \quad (1)$$

for the transverse component and

$$\mathbf{E}_\parallel(r, \theta, z; l, s) = E(r, z; l) \left[\frac{|l| - ls - 2r^2/w(z)^2}{kr} \right] \times \cos[\eta + (l + s)\theta] \hat{\mathbf{z}} \quad (2)$$

for the longitudinal component, where $\eta = kz + kr^2/(2R(z)) - (|l| + 1)\arctan(z/z_0)$. $w(z)$, $R(z)$, and z_0 refer to the beam waist, the curvature, and the Rayleigh range of the initial Gaussian pulse [37]. The common factor $E(r, z; l)$ is given as

$$E(r, z; l) = E_0 \left(\frac{w_0}{w(z)} \right) \left(\frac{\sqrt{2}r}{w(z)} \right)^{|l|} e^{-r^2/w(z)^2}, \quad (3)$$

where w_0 is the beam waist on the focal plane ($z = 0$). In the nomenclature of LG modes, l , an integer, is called an OAM number, and s , ± 1 for circularly polarized fields, is called a spin angular momentum number [19, 20]. These terms originate from the fact that, in the plane wave limit, the total AM of an LG pulse divided by the pulse energy equals $(l + s)/\omega$, where ω is the angular frequency of the pulse: a reminiscent of a photon cloud carrying a total AM of $N\hbar(l + s)$ and an energy of $N\hbar\omega$, where N is the number of photons in the cloud [20]. The initial Gaussian mode is represented by the formulas with $l = 0$.

The mathematical form of $E(r, z; l)$ in (3) implies that the transverse focal profile has a modulation in r : a Gaussian profile with $l = 0$ and a donut-shape profile with $|l| = 1$. In our study, we chose the LG pulses with $l = -s = 1$ so that the pulses have an inward ponderomotive force and have not transferred their AM to the protons after the interaction. In contrast, the LG pulses with $l = s = -1$ transfer a substantial amount of AM, and consequently the protons become significantly divergent. Furthermore, such LG pulses have a longitudinal electric field varying with θ , i.e. $(l + s)\theta$ in (2), which can hinder the formation of a uniform electron layer that is important in RPA. In our simulations, the LG pulses with $l = s = -1$ produced much poorer results than those with $l = -s = 1$, as anticipated. Also, note that, changing the

signs of l and s simultaneously does not bring any difference in the results, as far as proton acceleration is concerned. From now on, we refer to a pulse with $l = -s = 1$ by an LG pulse and to a pulse with $l = 0$ and $s = -1$ by a Gaussian pulse. In addition, we call the peak intensity of the initial Gaussian pulse the reference intensity, denoted by I_r ; the helical phase plates reduces the peak intensity by a factor of $1/e$ ($\simeq 0.37$) while retaining the pulse's power. The reference intensity varies from $I_r = 1.0 \times 10^{22} \text{ W cm}^{-2}$ to $I_r = 3.0 \times 10^{23} \text{ W cm}^{-2}$. As the temporal intensity profile of the laser pulses, we use a \sin^2 profile with a pulse duration (FWHM) of 20 fs. The laser wavelength is $\lambda = 800 \text{ nm}$, and the focal spot size $w_0 = 3 \mu\text{m}$.

As the plasma foil, we consider an electron-proton plasma with a density of $n_0 = 200n_c = 3.5 \times 10^{23} \text{ cm}^{-3}$, where n_c is the critical density for $\lambda = 800 \text{ nm}$. The thickness (d) of the foil is set to satisfy the optimum condition for RPA at a given reference intensity, i.e. $a = \pi\sigma$, where a is the normalized vector potential for I_r , and $\sigma = (d/\lambda)(n_0/n_c)$ [2, 5, 9]. For example, $d = 196 \text{ nm}$ for $I_r = 1.0 \times 10^{23} \text{ W cm}^{-2}$.

The simulations were carried out with the ALPS code, which has been used to study laser-particle acceleration [13, 38–40]. The simulation domain has a volume of $40 \mu\text{m}(x) \times 40 \mu\text{m}(y) \times 60 \mu\text{m}(z)$ and is divided into rectangular cells of which size is $20 \text{ nm}(x) \times 20 \text{ nm}(y) \times 5 \text{ nm}(z)$. Ten macro-particles for each species are assigned into a cell so that each macro-particle corresponds to 7×10^4 real particles, which is in the range of usual particle numbers adopted in RPA simulations [11, 41]. A laser field is launched on the xy plane at $z = z_{\min}$ according to the formula (1). The simulation was run from $t = 0 \text{ fs}$, when the front edge of the pulse reaches the target, to $t \geq 100 \text{ fs}$, when the pulse is well separated from the plasma.

In the intensity regime reaching $10^{23} \text{ W cm}^{-2}$, one may be concerned with the effect of radiation reaction on the acceleration process. In our simulations using a quantum electrodynamics module [42], however, radiation reaction had little effect on proton spectra, consistent with a previous study [43]. Although a significant damping was observed in the electron spectra above 30 MeV, the spectra below 30 MeV, occupying about 99% of the total electron population, were found almost intact like the proton spectra. This observation implies that these low-energy electrons are mainly responsible for proton acceleration. Thus, only the simulation results without radiation reaction are presented below.

3. Results and discussion

A striking difference in proton acceleration can occur when the driving Gaussian pulse is replaced by an LG pulse. As shown in figures 1(a) and (b), a high-density proton column is formed along the laser axis by the LG pulse, in contrast to an expanding proton bubble by the Gaussian pulse. More details are found from figures 1(c) and (d) that show the temporal evolution of the density profiles of the electrons and protons in the xz plane for the LG and Gaussian pulses, respectively.

For both cases, the electrons and protons in the target plasma are accelerated together. In figure 1(c), high-density electron and proton columns are formed around the laser axis, as the particles are pushed inward from the periphery. The high density at the laser axis is maintained, whereas, in the peripheral region, the density becomes low with a dispersed particle distribution. The plasma column is largely quasi-neutral, but the protons are more compressed in a narrower region, forming a column with a higher density than that of the electrons. In figure 1(d) showing a typical situation in the RPA process based on Gaussian pulses, the particle distribution bends outward first in accordance with the spatial distribution of the laser intensity, and then, as the acceleration develops, the target particles spread out with a decreasing density.

These different behaviors for the LG pulse and the Gaussian pulse can be anticipated from the spatial distribution of the radial ponderomotive force, $F_r \propto -\partial|\mathbf{E}_\perp|^2/\partial r$. From equations (1) and (3), the LG pulse has $-\partial|\mathbf{E}_\perp|^2/\partial r = 2|\mathbf{E}_\perp|^2(2r^2/w_0^2 - 1)/r$ on the focal plane, according to which the ponderomotive force is focusing in the region with $r < w_0/\sqrt{2}$ and defocusing in the region with $r > w_0/\sqrt{2}$. In the focusing region, the electrons are pushed toward the laser axis firstly due to their small mass, and, then, the resulting Coulomb field due to the charge separation tugs the protons. Consequently, the whole plasma in the region is compressed toward the laser axis. In contrast, the Gaussian pulse has $-\partial|\mathbf{E}_\perp|^2/\partial r = 4|\mathbf{E}_\perp|^2 r/w^2$, and only a defocusing ponderomotive force is available in this case, resulting in a dispersing plasma cloud. Thus the proton jet shown in figure 1(a) is attributed to the combined action of radial compression and forward acceleration.

The forward acceleration of protons can be readily identified in their density evolution around the laser beam waist $r = w_0/\sqrt{2} = 2.1 \mu\text{m}$, where the LG pulse has an intensity peak (figure 1(c)). During the early interaction phase, $t \leq 20 \text{ fs}$, both the electrons and protons show highly peaked densities, forming thin layers. The maximum density of the proton increases by more than three times the initial density. At approximately 30 fs, the high-density layers are broadened to a density lower than the initial density. The propagation of two almost overlapping layers of electrons and protons indicates that the RPA of the target material actually takes place. The ‘double-layer’ structure, which is a typical RPA characteristic [44, 45], can be clearly identified in figure 1(c). This double-layer structure is well maintained up to $t = 40 \text{ fs}$, and afterwards it begins to be smeared. The termination of the RPA occurs due to the combination of a few processes such as separation of the pulse from the plasma, relativistic transparency, target surface bending, and the Rayleigh–Taylor instability [14]; the last can be suppressed for double-ion-species targets [46]. The termination processes are very similar to each other between the two cases of the LG and Gaussian pulses, as shown in figures 1(c) and (d). In fact, this kind of loss in the double-layer structure is one of the major factors limiting the RPA based on the laser-matter interaction.

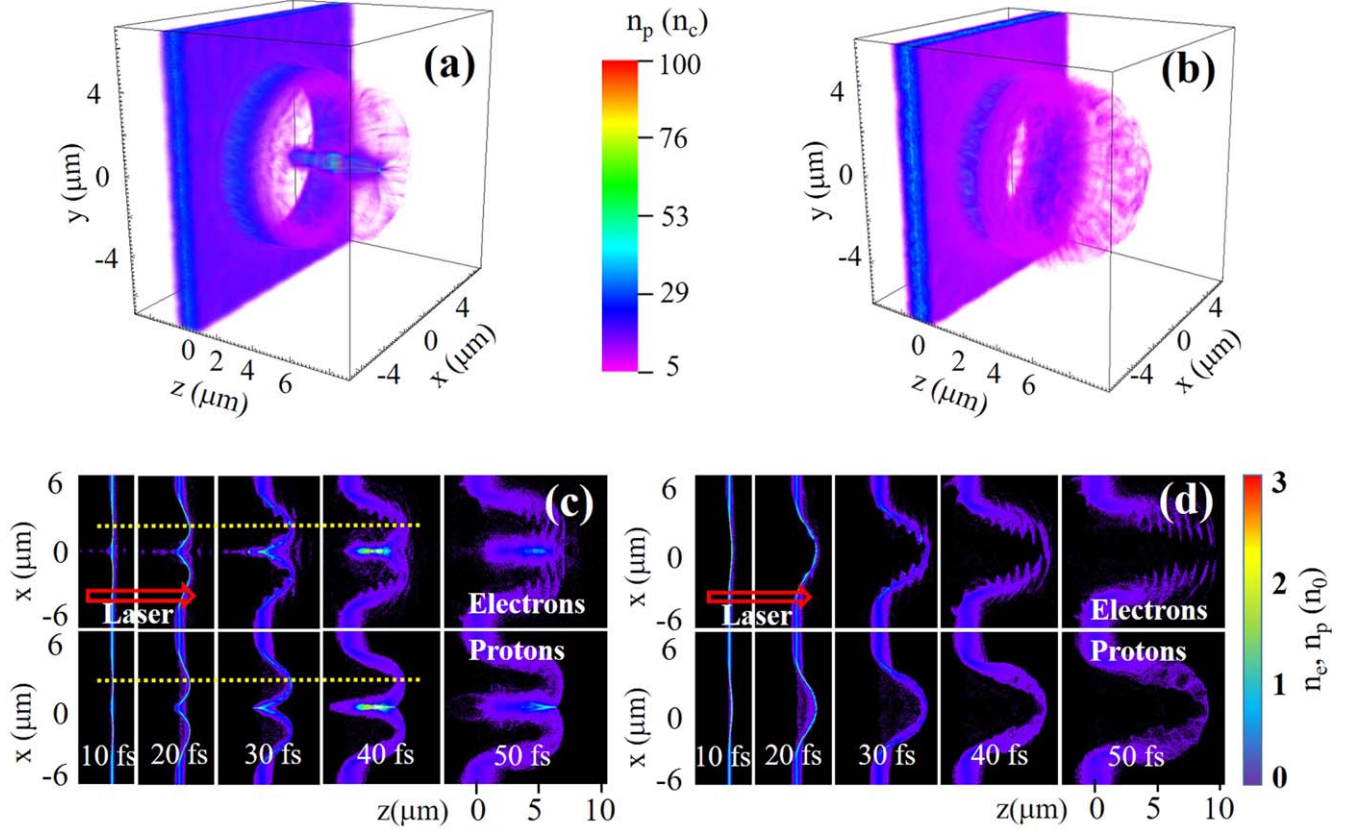


Figure 1. Proton acceleration by an LG pulse compared with that by the corresponding Gaussian pulse. Proton density distributions at $t = 60$ fs for (a) the LG pulse and (b) the Gaussian pulse. Density evolution of the electrons (upper) and protons (lower) in time for (c) the LG pulse and (d) the Gaussian pulse. The laser pulses propagate from left to right. The yellow dotted lines in (c) denote the radial positions of the maximum intensity: $r = w_0/\sqrt{2} = 2.1 \mu\text{m}$. The reference intensity is $I_r = 1.0 \times 10^{23} \text{ W cm}^{-2}$. As the pulse duration is only 20 fs (FWHM), the evolution after $t = 50$ fs is largely a plasma relaxation.

Further details about the compression and acceleration processes by the LG pulse can be understood from the density and momentum distributions. The proton density profile in the xz plane ($y = 0$) at time $t = 20$ fs is shown in figure 2(a), along with the profile of $|\mathbf{E}|^2$ on the focal plane (the xy plane at $z = 0$). At this moment, the intensity peak of the laser pulse arrives at the initial position of the target front. Comparing the curve of $|\mathbf{E}|^2$ to the density map, we find that the stronger $|\mathbf{E}|^2$ is, the further the protons are pushed forward, and the higher the density is. This is because the longitudinal ponderomotive force is roughly proportional to $-\partial_z |\mathbf{E}|^2 \sim |\mathbf{E}|^2/d$ for the used laser and target parameters. The good correlation between the laser intensity profile and the proton density distribution supports the view that the proton acceleration mainly arises from the radiation pressure, which is proportional to the intensity.

More specifically, we compare the protons accelerated around the intensity peak and those accelerated in the intensity downhill, corresponding to the high-density regions in (i) and (ii) in figure 2(a), respectively. Seeing the strongest longitudinal ponderomotive force, the protons around $x = \pm 1.8 \mu\text{m}$ in (i) are pushed the farthest (figure 2(a)) and strongly squeezed in the longitudinal direction to a density more than double the initial density (figure 2(b)). They also acquire a high longitudinal momentum (figure 2(d)). Among

them, the protons within a radius of $r \simeq 1.7 \mu\text{m}$ have small negative radial momenta (figure 2(c)), and these protons will gather slowly around the axis in the ensuing acceleration process. In contrast, the protons around $x = \pm 0.7 \mu\text{m}$ and $x = \pm 3.0 \mu\text{m}$ in (ii) see a weaker longitudinal ponderomotive force but a stronger radial ponderomotive force than the protons in (i) do. As a result, those protons are pushed to a shorter distance in the forward direction (figure 2(a)) with a lower density (figure 2(b)) and lower longitudinal momenta (figure 2(d)). Among them, the protons within a radius of $r \simeq 1.0 \mu\text{m}$ have a larger negative radial momentum and will gather around the axis quickly. Although the radial ponderomotive force is negative from the position of $r = w_0/\sqrt{2} = 2.1 \mu\text{m}$ and inward, the plasma fields should make the protons in (i) and (ii) have negative radial momenta from the position of a smaller radius.

The remarkable advantage of using an LG laser pulse appears clearly in the energy spectrum. Figure 3(a) shows the proton energy spectra at $t = 200$ fs by the LG pulse and the Gaussian pulse. At $t = 100$ fs, the laser pulse is already separated well from the plasma. When the emission angle is limited to 1° , the maximum proton energy (940 MeV) for the LG pulse is 75% of that for the Gaussian pulse, but the number of protons per unit energy is 20–100 times larger for the energy between 300 and 900 MeV. In the LG pulse case,

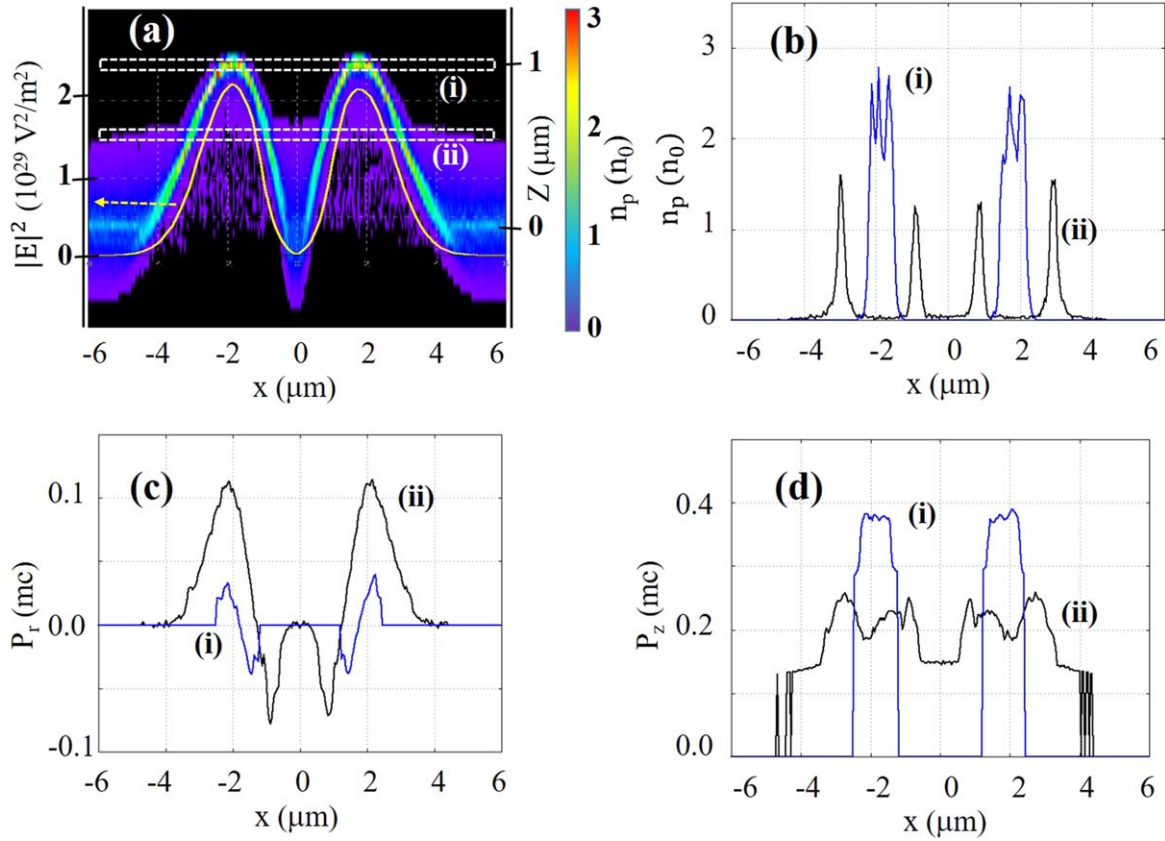


Figure 2. Density and momentum distribution of protons at $t = 20$ fs. (a) The density map in the xz plane ($y = 0$) overlapped with the profile of $|E|^2$ on the focal plane (yellow line); cut views along the lines (i) and (ii) in (a): (b) the proton density, (c) the radial momentum, and (d) the longitudinal momentum. In (a), the vertical scale for $|E|^2$ is set so to make the curve of $|E|^2$ fitted to the proton density map. P_r and P_z denote the average momentum of the particles within a small region around x . Note that the figures have a good cylindrical symmetry with respect to the laser axis.

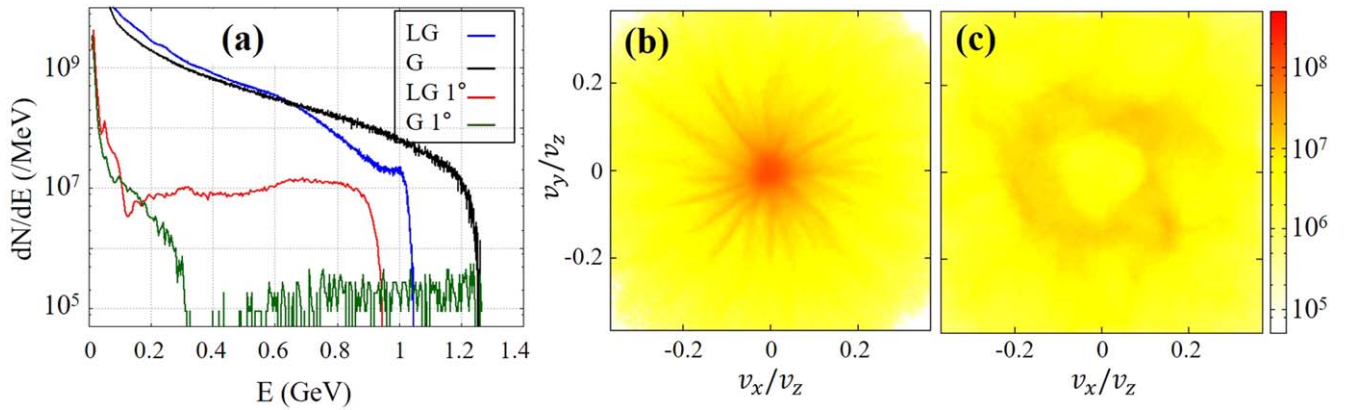


Figure 3. Energy spectra and angular distributions of the protons in the LG pulse case and in the Gaussian pulse case at an intensity of $I_r = 1.0 \times 10^{23} \text{ W cm}^{-2}$ ($t = 200$ fs). (a) Proton spectra with and without limiting the emission angle to 1° ; angular distributions of high-energy (>400 MeV) protons (b) in the LG pulse case and (c) in the Gaussian pulse case.

the integrated number of protons is 7.0×10^9 for the energy above 200 MeV, whereas 3.0×10^8 protons are counted in the Gaussian pulse case above 200 MeV. The lower maximum proton energy for the LG pulse may be attributed to the fact that the peak intensity is reduced when the Gaussian pulse is

converted into an LG pulse by a helical phase plate (section 2). Although the maximum energy of the proton is smaller, the much enhanced spectral intensity makes the LG acceleration scheme very attractive for producing a dense low-divergence proton jet, which may obviate heavy focusing

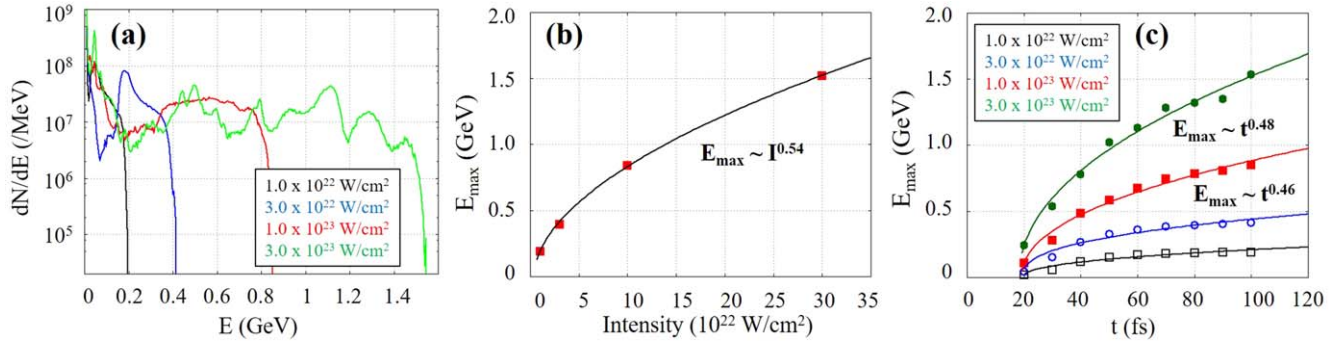


Figure 4. Spectra and maximum energies of the protons having an emission angle smaller than 1° for various laser intensities of the LG pulse: (a) proton energy spectra at $t = 100$ fs; (b) maximum proton energy at $t = 100$ fs; (c) time evolution of the maximum proton energy. The target thickness is set to satisfy the RPA optimum condition $a = \pi\sigma$ for each reference laser intensity: 62 nm for $I_r = 1.0 \times 10^{22} \text{ W cm}^{-2}$, 104 nm for $I_r = 3.0 \times 10^{22} \text{ W cm}^{-2}$, 196 nm for $I_r = 1.0 \times 10^{23} \text{ W cm}^{-2}$, and 336 nm for $I_r = 3.0 \times 10^{23} \text{ W cm}^{-2}$. The fitting curves in (b) and (c) are obtained by the least-square fit method: in (b), $E_{\text{max}} = 0.25 \times (I_r/10^{22} \text{ W cm}^{-2}) - 0.42)^{0.54}$; in (c), $E_{\text{max}} = 0.032 \times (t - 20)^{0.43}$ for $I_r = 1.0 \times 10^{22} \text{ W cm}^{-2}$, $E_{\text{max}} = 0.082 \times (t - 20)^{0.38}$ for $I_r = 3.0 \times 10^{22} \text{ W cm}^{-2}$, $E_{\text{max}} = 0.12 \times (t - 19)^{0.46}$ for $I_r = 1.0 \times 10^{23} \text{ W cm}^{-2}$, and $E_{\text{max}} = 0.18 \times (t - 18)^{0.48}$ for $I_r = 3.0 \times 10^{23} \text{ W cm}^{-2}$, where E_{max} is in units of GeV, and t in units of fs.

equipment in applications. When the emission angle is not limited, the Gaussian pulse achieves a higher maximum energy (1240 MeV) and a higher yield for the energy above 650 MeV, but the yield of the LG pulse is higher below 650 MeV.

The divergence of the proton jet can be estimated from the angular distribution obtained much after the termination of the laser-target interaction. Figures 3(b) and (c) show the angular distributions of the high-energy (>400 MeV) protons at $t = 200$ fs in the LG pulse case and in the Gaussian pulse case, respectively. As the laser pulse is separated well from the plasma before $t = 100$ fs, it may be reasonable to assume a ballistic propagation afterward, e.g. after $t = 200$ fs. Then the figures can be considered as numerical far-field beam patterns, which can be compared with experimental beam patterns. In the case of the LG pulse, the accelerated protons have a very low divergence angle due to the compression. In contrast, for the Gaussian pulse, the protons are distributed in a broader ring with only a tiny number of protons in the laser propagation direction. In the Gaussian case, as the laser intensity profile has a peak at the center of the beam cross-section, the ponderomotive force drives the particles to diverge radially. The ultimate numerical confirmation of such ballistic propagation needs 3D PIC simulations over a much extended space and time, which are hardly found in the literature [1, 2].

To understand the dependence on laser intensity, proton energy spectrum and maximum proton energy are investigated for laser intensities from 1.0×10^{22} to $3.0 \times 10^{23} \text{ W cm}^{-2}$ (figure 4). The target thickness is set to satisfy the RPA optimum condition $a = \pi\sigma$ for each reference intensity; consequently, the target mass increases proportional to $I^{0.5}$. In figure 4(a), the number of protons per unit energy, dN/dE , is in the range of 10^7 – 10^8 up to the maximum proton energy and is not appreciably affected by the increase of laser intensity. In contrast, the maximum proton energy E_{max} increases proportional to $I^{0.54}$ (figure 4(b)). It is close to the scaling $E_{\text{max}} \sim I^{0.5}$ that is predicted by the 1D analytic model of RPA when the optimum condition $a = \pi\sigma$ is maintained, and the radiation flux is sufficiently high [2]. The

horizontal extension of plateau in figure 4(a) can be considered as a characteristic merit of the RPA: an increased laser momentum is efficiently used to generate higher-energy protons without increasing low-energy protons. Figure 4(c) shows the increase of the maximum proton energy in time, in which the scaling exponent varies from 0.38 to 0.48. These values are close to the predictions from the analytical models of RPA: the 1D light-sail model predicts an exponent of $1/3$ [2, 3], and the 3D model including transverse expansion predicts an exponent of $3/5$ [47]. The dependence on laser intensity shown in figure 4 supports that the proton acceleration with the LG pulses occurs in the regime of RPA.

For particle accelerators, beam emittance is an important parameter measuring the spread in position-momentum phase space, and thus we estimated it with the protons at $t = 200$ fs. The transverse normalized rms emittance is defined for a group of particles having a fixed energy as follows [48]:

$$\epsilon_{nx} = \beta\gamma\sigma_x\sigma_{x'}\sqrt{1 - \rho_{xx'}^2}, \quad (4)$$

where β and γ are the relativistic parameters for the proton energy, $x' = dx/dz = p_x/p_z$, σ_x the standard deviation of x , $\sigma_{x'}$ the standard deviation of x' , and $\rho_{xx'}$ the correlation coefficient of x and x' . Figure 5(a) shows the emittance as a function of the proton energy for the cases of the LG and Gaussian pulses. The emittance values are largely similar in magnitude in the two cases (except near the lowest energies): as the energy increases from 0.1 GeV to about 1 GeV, the emittance decreases from about $0.5 \mu\text{m}$ to about $0.05 \mu\text{m}$. These values are smaller by an order of magnitude than those of conventional proton accelerators. This similarity is surprising because the LG pulse produces a transversely confined proton jet with a smaller divergence. For example, for the protons with an energy from 700 to 710 MeV, the standard deviations of x and x' are almost doubled in the Gaussian pulse case: $\sigma_x = 7.73 \mu\text{m}$ and $\sigma_{x'} = 0.222$ in the Gaussian pulse case, and $\sigma_x = 4.06 \mu\text{m}$ and $\sigma_{x'} = 0.107$ in the LG pulse case. However, the correlation coefficient is slightly smaller in the LG pulse case, $\rho_{xx'} = 0.976$ versus $\rho_{xx'} = 0.999$, which leads to comparable emittance values: $\epsilon_{nx} = 0.134 \mu\text{m}$ in the LG pulse case and $\epsilon_{nx} = 0.0989 \mu\text{m}$ in the Gaussian pulse

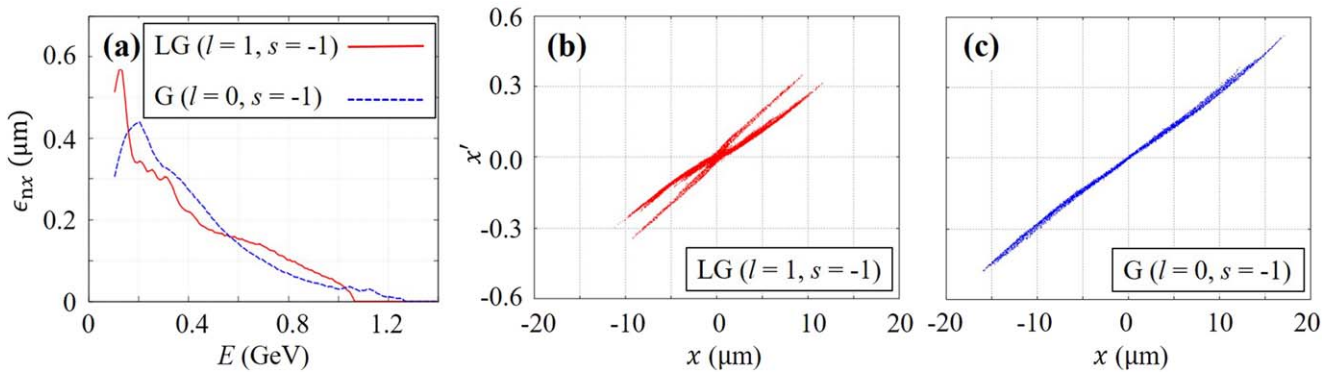


Figure 5. Beam emittance and trace space distributions of protons at $t = 200$ fs. (a) Beam emittance as a function of proton energy in the LG pulse case and in the Gaussian pulse case. For a given energy value, the protons within an energy interval of 10 MeV were taken into account to estimate the emittance. Trace space ($x' = p_x/p_z$) distribution of the protons with energies between 700 MeV and 710 MeV (b) in the LG pulse case and (c) in the Gaussian pulse case.

case. The smaller correlation coefficient is attributed to the double-branch structure in the trace space shown in figure 5(b). Compared with the single-branch structure in figure 5(c), the double-branch structure has a smaller modulus of correlation coefficient. A further study is necessary to identify the origin of the double-branch structure.

Lastly we discuss briefly the requirements for experiments. The foremost requirement is a donut-shape beam profile, which is formed by a single LG mode in our simulations. In practice, however, only a combination of LG modes are available because helical phase plates have a stepwise thickness variation. According to Sueda *et al* [49], about 78% of pulse energy can be put into a single LG mode when the steps for a thickness of one laser wavelength are over 16. In their experiments, even with a low modal purity of 55%, a clear donut-shape profile was obtained. However, such phase plates cannot be used for petawatt laser pulses due to optical damage and pulse distortion, and thus phase mirrors are being developed by using a high-precision diamond turning machine.

Another requirement is a steep plasma profile, which is the prerequisite of the RPA scheme. Prepulses and pulse pedestals should be removed not to have an extended preplasmas when the main part of a laser pulse arrives. Typically plasma mirrors are used to remove them [50]. A pulse contrast of 10^{11} or higher can be obtained [51], and the theoretically predicted features of RPA have been demonstrated in experiments by using plasma mirrors [10–13]. Meeting both requirements with petawatt pulses can be a challenging task, but we may be optimistic, considering the relentless progress in optical and mechanical technologies.

4. Conclusion

Directed proton acceleration to GeV energy was examined using LG pulses with intensities in the range of 10^{22} – 10^{23} W cm^{-2} . The acceleration of protons and ions with such ultra-high intensity lasers is expected to reach relativistic energy. As multi-PW lasers are operational or expected to operate in a number of laser facilities, proton acceleration at such intensities by the radiation pressure mechanism can be examined in the near future. The scheme proposed here can pave a pathway to greatly

improve the quality of proton beams accelerated to relativistic energy.

To conclude, the proton acceleration scheme using an ultra-intense circularly polarized LG laser pulse irradiating a thin film target has been proposed as a novel mechanism to generate a high-density high-energy proton jet. From 3D PIC simulations, it was demonstrated that a low-divergence high-density relativistic proton jet can be generated, and the number of high-energy protons can increase by a factor of more than tens for an emission angle smaller than 1° , as compared with the case of Gaussian laser pulses. We emphasize here the generation of a low-divergence GeV proton beam, drastically different from the proton acceleration with a Gaussian laser pulse, since the production of such a collimated high energy proton beam makes this scheme very attractive for future high-power laser-driven ion accelerators.

Acknowledgments

This work was supported by IBS (Institute for Basic Science) under IBS-R012-D1 and by GIST Research Institute (GRI). CMK thanks Dr Peter Nickles for his valuable comments.

ORCID iDs

Ki Hong Pae <https://orcid.org/0000-0003-4363-9624>
Hoon Song <https://orcid.org/0000-0001-8683-7546>
Chang-Mo Ryu <https://orcid.org/0000-0001-6264-5152>
Chang Hee Nam <https://orcid.org/0000-0001-8203-0702>
Chul Min Kim <https://orcid.org/0000-0002-0417-6519>

References

- [1] Daido H, Nishiuchi M and Pirozhkov A S 2012 *Rep. Prog. Phys.* **75** 056401
- [2] Macchi A, Borghesi M and Passoni M 2013 *Rev. Mod. Phys.* **85** 751

- [3] Esirkepov T, Borghesi M, Bulanov S V, Mourou G and Tajima T 2004 *Phys. Rev. Lett.* **92** 175003
- [4] Qiao B, Kar S, Geissler M, Gibbon P, Zepf M and Borghesi M 2012 *Phys. Rev. Lett.* **108** 115002
- [5] Macchi A, Cattani F, Liseykina T V and Cornolti F 2005 *Phys. Rev. Lett.* **94** 165003
- [6] Zhang X, Shen B, Li X, Jin Z, Wang F and Wen M 2007 *Phys. Plasmas* **14** 123108
- [7] Klimo O, Psikal J, Limpouch J and Tikhonchuk V 2008 *Phys. Rev. Spec. Top.—Accel. Beams* **11** 031301
- [8] Robinson A, Zepf M, Kar S, Evans R and Bellei C 2008 *New J. Phys.* **10** 013021
- [9] Yan X Q, Lin C, Sheng Z M, Guo Z Y, Liu B C, Lu Y R, Fang J X and Chen J E 2008 *Phys. Rev. Lett.* **100** 135003
- [10] Henig A *et al* 2009 *Phys. Rev. Lett.* **103** 245003
- [11] Steinke S *et al* 2013 *Phys. Rev. ST* **16** 011303
- [12] Kar S *et al* 2012 *Phys. Rev. Lett.* **109** 185006
- [13] Kim I J *et al* 2016 *Phys. Plasmas* **23** 070701
- [14] Pegoraro F and Bulanov S V 2007 *Phys. Rev. Lett.* **99** 065002
- [15] Qiao B, Zepf M, Gibbon P, Borghesi M, Dromey B, Kar S, Schreiber J and Geissler M 2011 *Phys. Plasmas* **18** 043102
- [16] Bulanov S S, Esarey E, Schroeder C B, Bulanov S V, Esirkepov T Zh, Kando M, Pegoraro F and Leemans W P 2016 *Phys. Plasmas* **23** 056703
- [17] Bulanov S V, Wilkens J J, Esirkepov T Z, Korn G, Kraft G, Kraft S D, Molls M and Khoroshkov V S 2014 *Phys. Usp.* **57** 1149
- [18] Miyazaki S, Kawata S, Kong Q, Miyauchi K, Sakai K, Hasumi S, Sonobe R and Kikuchi T 2005 *J. Phys. D: Appl. Phys.* **38** 1665
- [19] Padgett M, Courtial J and Allen L 2004 *Phys. Today* **57** 35–40
- [20] Torres J P and Torner L 2011 *Twisted Photons: Applications of Light with Orbital Angular Momentum* (Weinheim: Wiley-VCH)
- [21] Allen L, Beijersbergen M W, Spreeuw R J C and Woerdman J P 1992 *Phys. Rev. A* **45** 8185
- [22] Padgett M J 2017 *Opt. Express* **25** 11265–74
- [23] He H, Frieze M E J, Heckenberg N R and Rubinsztein-Dunlop H 1995 *Phys. Rev. Lett.* **75** 826
- [24] Zhang X M, Shen B F, Shi Y, Wang X F, Zhang L G, Wang W P, Xu J C, Yi L Q and Xu Z Z 2015 *Phys. Rev. Lett.* **114** 173901
- [25] Denoeud A, Chopineau L, Leblanc A and Quéré F 2017 *Phys. Rev. Lett.* **118** 033902
- [26] Leblanc A, Denoeud A, Chopineau L, Mennerat G, Martin P and Quéré F 2017 *Nat. Phys.* **13** 440–3
- [27] Harwit M 2003 *Astrophys. J.* **597** 1266–70
- [28] Tamburini F, Thidé B, Molina-Terriza G and Anzolin G 2011 *Nat. Phys.* **7** 195
- [29] Sizyuk V, Hassanein A and Sizyuk T 2007 *Laser Part. Beams* **25** 143–54
- [30] Zhang X, Shen B, Zhang L, Xu J, Wang X, Wang W, Yi L and Shi Y 2014 *New J. Phys.* **16** 123051
- [31] Hu L X, Yu T P, Li H Z, Yin Y, McKenna P and Shao F Q 2018 *Opt. Lett.* **43** 2615–8
- [32] Hu L X, Yu T P, Sheng Z M, Vieira J, Zou D B, Yin Y, McKenna P and Shao F Q 2018 *Sci. Rep.* **8** 1–9
- [33] Hu L X, Yu T P, Lu Y, Zhang G B, Zou D B, Zhang H, Ge Z Y, Yin Y and Shao F Q 2018 *Plasma Phys. Control. Fusion* **61** 025009
- [34] Brabetz C, Busold S, Cowan T, Deppert O, Jahn D, Kester O, Roth M, Schumcher D and Bagnoud V 2015 *Phys. Plasmas* **22** 013105
- [35] Shi Y, Shen B F, Zhang L G, Zhang X M, Wang W P and Xu Z Z 2014 *Phys. Rev. Lett.* **112** 235001
- [36] Gbur G J 2011 *Mathematical Methods for Optical Physics and Engineering* (Cambridge: Cambridge University Press)
- [37] Milonni P W and Eberly J H 2010 *Laser Physics* (New York: Wiley)
- [38] Pae K H, Choi I W and Lee J 2010 *Phys. Plasmas* **17** 123104
- [39] Kim I J *et al* 2013 *Phys. Rev. Lett.* **111** 165003
- [40] Pae K H, Kim C M and Nam C H 2016 *Phys. Plasmas* **23** 033117
- [41] Yu T, Sheng Z, Pukhov A, Yin Y, Zhuo H, Ma Y, Xu X, Shao F and Zhou C 2013 *Plasma Phys. Control. Fusion* **55** 085021
- [42] Gonoskov A, Bastrakov S, Efimenko E, Ilderton A, Marklund M, Meyerov I, Muraviev A, Sergeev A, Surmin I and Wallin E 2015 *Phys. Rev. E* **92** 023305
- [43] Tamburini M, Pegoraro F, Di Piazza A, Keitel C H and Macchi A 2010 *New J. Phys.* **12** 123005
- [44] Macchi A, Vaghini S and Pegoraro F 2009 *Phys. Rev. Lett.* **103** 085003
- [45] Qiao B, Zepf M, Borghesi M, Dromey B, Geissler M, Karmakar A and Gibbon P 2010 *Phys. Rev. Lett.* **105** 155002
- [46] Yu T P, Pukhov A, Shvets G and Chen M 2010 *Phys. Rev. Lett.* **105** 065002
- [47] Bulanov S V, Echkin E Yu, Esirkepov T Zh, Inovenkov I N, Kando M, Pegoraro F and Korn G 2010 *Phys. Rev. Lett.* **104** 135003
- [48] Reiser M 2008 *Theory and Design of Charged Particle Beams* 2nd edn (Weinheim: Wiley-VCH)
- [49] Sueda K, Miyaji G, Miyanaga N and Nakatsuka M 2004 *Opt. Express* **12** 3548
- [50] Doumy G, Quéré F, Gobert O, Perdrix M, Martin P, Audebert P, Gauthier J, Geindre J P and Wittmann T 2004 *Phys. Rev. E* **69** 026402
- [51] Kim I, Choi I, Lee S, Janulewicz K, Sung J, Yu T, Kim H, Yun H, Jeong T and Lee J 2011 *Appl. Phys. B* **104** 81–6